The Role of Fault–Zone Architectural Elements on Pore Pressure Propagation and Induced Seismicity

by John P. Ortiz[1], Mark A. Person[2], Peter S. Mozley[2], James P. Evans[3], and Susan L. Bilek[2]

Abstract

We used hydrogeologic models to assess how fault-zone properties promote or inhibit the downward propagation of fluid overpressures from a basal reservoir injection well (150 m from fault zone, $Q = 5000 \, \text{m}^3/\text{day}$) into the underlying crystalline basement rocks. We varied the permeability of the fault-zone architectural components and a crystalline basement weathered layer as part of a numerical sensitivity study. Realistic conduit-barrier style fault zones effectively transmit elevated pore pressures associated with 4 years of continuous injection to depths of approximately 2.5 km within the crystalline basement while compartmentalizing fluid flow within the injection reservoir. The presence of a laterally continuous, relatively low-permeability altered/weathered basement horizon ($k_{\text{altered layer}} = 0.1 \times k_{\text{basement}}$) can limit the penetration depth of the pressure front to approximately 500 m. On the other hand, the presence of a discontinuous altered/weathered horizon that partially confines the injection reservoir without blocking the fault fluid conduit promotes downward propagation of pressures. Permeability enhancement via hydromechanical failure was found to increase the depth of early-time pressure front migration by a factor of 1.3 to 1.85. Dynamic permeability models may help explain seismicity at depths of greater than 10 km such as is observed within the Permian Basin, NM.

Introduction

The link between wastewater reinjection into basal reservoirs—that is, reservoir formations located directly on top of basement rocks—and triggered seismicity within the underlying crystalline basement has been documented at a number of sites, including Ohio, with injection into the basal Mt. Simon Sandstone (Nicholson and Wesson 1990; Kim 2013), New Mexico Permian Basin; with injection into the basal Ellenburger Limestone (Zhang et al. 2016), Oklahoma; with injection into the basal Arbuckle Limestone (Keranen et al. 2013, 2014; Walsh and Zoback 2015, 2016; Yeck et al. 2016), Texas Fort Worth Basin; with injection into the Ellenburger Limestone (Hornbach et al. 2015), Kansas; with injection into the Arbuckle Limestone (Choy et al. 2016), and Arkansas; with injection into the basal Ozark Aquifer (Horton 2012). Earthquake hypocenters occur at a wide range of depths (typically 2 to 8 km) below the injection reservoir within the underlying crystalline basement (Table 1), sometimes at significant lateral distances (greater than 10 km) from injection wells (Keranen et al. 2014; Zhang et al. 2016). Although wellhead injection pressures can be relatively high, the estimated increases in hydraulic head where triggered seismicity occurs within the crystalline basement—up to tens of kilometers from the well screen—are much lower. Hsieh and Bredehoeft (1981) found that the pressure increase threshold associated with induced seismicity at the Rocky Mountain Arsenal in Colorado was 320 m of hydraulic head ($\sim$3.2 MPa) at an average depth of 5 km; Keranen et al. (2014) used hydrologic models to conclude that a head increase of only 7 m ($\sim$0.07 MPa) was consistent with induced seismicity within the crystalline basement in central Oklahoma.

Relocation studies of earthquake hypocenters associated with crystalline basement seismicity suggest that fluid migration can occur along conductive sub-vertical fault zones (e.g., Shapiro et al. 1997; Horton 2012; Zhang et al. 2016). Faults can act as barriers or conduits to fluid flow (e.g., Antonellini and Aydin 1995; Caine et al. 1996)

---

[1]Corresponding author: Computational Earth Science Group, Los Alamos National Laboratory, Los Alamos, NM 87544; 541 207 5846; jportiz@lanl.gov
[2]Department of Earth & Environmental Science, New Mexico Institute of Mining and Technology (New Mexico Tech), Socorro, NM, 87801; markaustinperson@gmail.com; psmozley@gmail.com; susan.bilek@nmt.edu
[3]Department of Geology, Utah State University, Logan, UT, 84322; james.evans@usu.edu

Table 1

Injection, Seismicity, and Fluid Pressure Data from Case Studies Documenting Instances of Induced Seismicity Across the USA

Location	Basal Reservoir Name	Maximum Earthquake Magnitude/Average Hypocenter Depth (km)	Maximum Cumulative Injection Rate (m³ d⁻¹)	Maximum Depth of Seismicity Below Injection Wells (km)
Jones, OK[1,4]	Arbuckle Limestone	3/4.5	95,392	3.75
Guy, AR[2]	Ozark Aquifer	4.7/5	9,539	5.2
Prague, OK[3]	Arbuckle Limestone	5.7/5	3,180	7
Dagger Draw, NM[5]	Ellenburger Limestone	3.2/11	15,899	8.65
Rocky Mtn Arsenal, CO[6]	Crystalline basement	5.5/5	1,007	3.5
Azle, TX[7]	Ellenburger Limestone	3.6/5	6,467	5
Milan, KS[8]	Arbuckle Limestone	4.9/6	2,332	4
Fairview, OK[9]	Arbuckle Limestone	5.1/7.5	100,692	6.5

Note: Cumulative injection refers to the summed injection rates of all wells within a given area.
[1]Keranen et al. (2014).
[2]Horton (2012).
[3]Keranen et al. (2013).
[4]Walsh and Zoback (2015).
[5]Zhang et al. (2016).
[6]Hsieh and Bredehoeft (1981).
[7]Hornbach et al. (2015).
[8]Choy et al. (2016).
[9]Yeck et al. (2016).

or as conduit-barrier systems (Bense and Person 2006). Previous work has conceptualized fault-related fluid flow based on fault zone architectural elements (e.g., Caine et al. 1996; Evans et al. 1997). Faults zones can include a low-permeability fault core, where the majority of slip is accommodated, and high-permeability damage zones, which are mechanically related to the growth of the fault (Forster and Evans 1991; Caine et al. 1996). The proportion of these components in a given fault zone varies (Antonellini and Aydin 1995; Caine et al. 1996; Evans et al. 1997) and affects the hydraulic structure of faults (Bense and Person 2006).

We assess how fault zone architectural elements influence fluid pressure propagation from basal injection reservoirs into crystalline basement rocks using a suite of idealized three-dimensional models in which the hydrogeological properties of fault core and damage zone permeability are systematically varied. We determine whether realistic hydrogeologic architecture (e.g., a damage zone width of about 10 m) produces downward propagation of pore pressures to depths of 2 to 8 km consistent with field observations of triggered seismicity. We also test the effect of a thin, relatively low permeability altered basement zone. Recent field studies focusing on the bedrock-sedimentary basin interface revealed the presence of an altered/weathered basement zone up to 20 m thick in some locations (Kerner et al. 2015; Cuccio 2017) that has lower permeability than the surrounding rocks. We also explore the effect of dynamic permeability enhancement (Rojstaczer et al. 2008) on downward propagation of pore pressures using a simple cross sectional model. This dynamic model allows permeability increases to be triggered when pore pressures increase above some threshold value.

We address the following questions in this study using hydrologic modeling:

1. Can realistic fault-zone architectural elements explain downward fluid pressure propagation into crystalline basement rock to depths of 2 to 8 km, consistent with reports of triggered seismicity?
2. How wide and permeable does the damage zone need to be to promote downward propagation of pore pressures?
3. What effect does an altered basement zone have on hydrogeologic conditions within the crystalline basement?
4. How does dynamic permeability enhancement in response to excess fluid pressure influence the patterns and depths of the pressure envelope?

Background

Data from deep crystalline basement borehole tests indicate that average intrinsic permeability of the rock (k or permeability herein) ranges from 10^{-16} to 10^{-14} m² to depths of approximately 4 km, with extremes varying from 10^{-19} to 10^{-12} m² (Mazurek 1998; Stober and Bucher 2006, 2015; Ranjram et al. 2015). A general permeability decay relationship (Figure 1) based on heat flow and metamorphic studies is

$$\log k = -3.2 \log z - 14, \tag{1}$$

where depth z is in km and permeability k is in m², predicting a value of k approximately 1×10^{-18} m² in the ductile crust at approximately 12 to 14 km depth (Manning and Ingebritsen 1999). Other studies have found
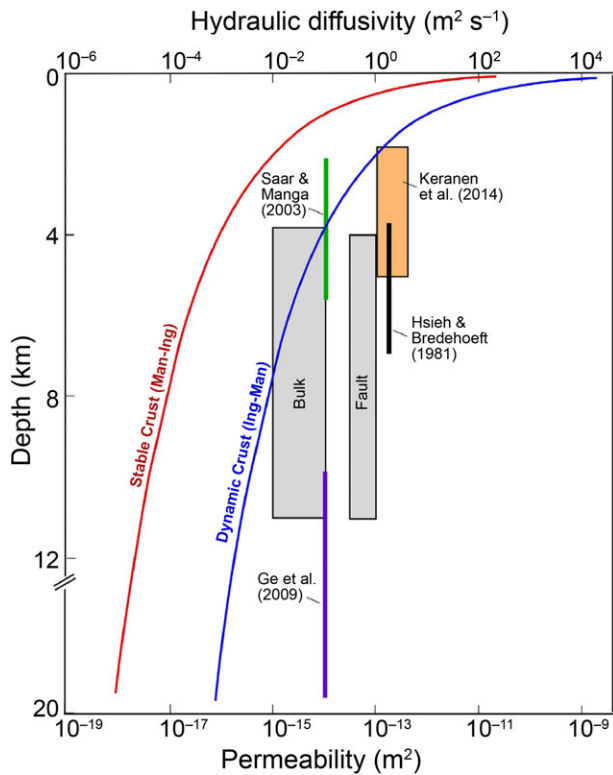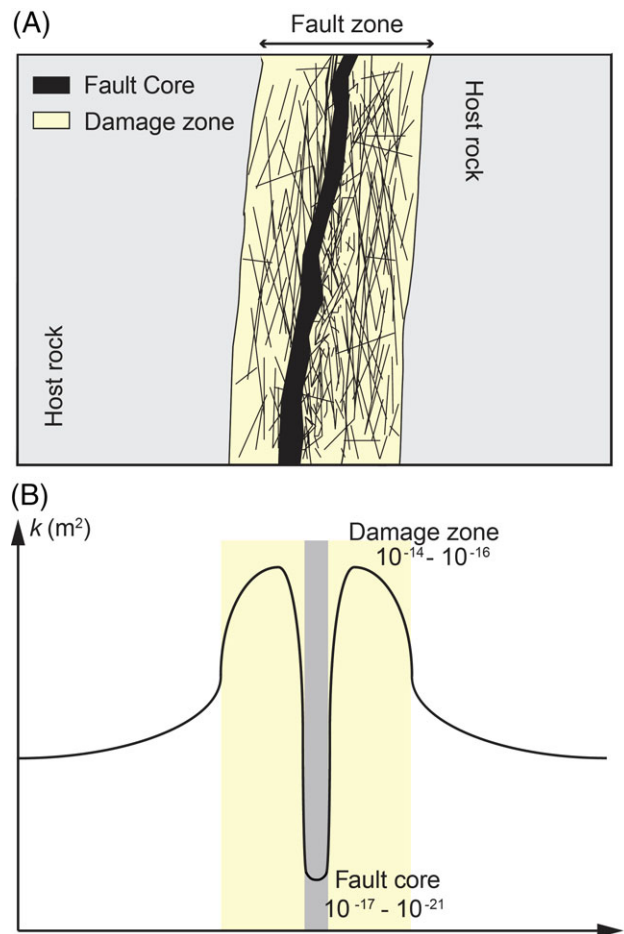
Figure 1. Hydraulic diffusivities and permeabilities derived from model reconstructions of triggered seismicity studies (boxes and vertical lines) and crustal permeability trends inferred from geophysical, petrological, and geophysical data (red and blue lines). The red permeability-depth curve is from Manning and Ingebritsen (1999). The blue permeability decay curve is from Ingebritsen and Manning (2010). The permeability axis assumes a specific storage coefficient of 10^{-6}/m. The gray boxes are permeabilities reported by Zhang et al. (2016) for the Dagger Draw oil field in southeastern New Mexico (Figure from Zhang et al. 2016).

Figure 2. (A) View of typical fault zone architectural components including undeformed host rock, fractured damage zone, and central fault core. (B) Conceptual plot of order-of-magnitude permeability variation across along an imaginary transect across the above fault zone showing increased permeability in the damage zone (yellow) and reduced permeability in the fault core (gray) (Adapted from Rinaldi et al. 2014).

permeability increases in narrowly defined regions. Evans et al. (2005) found that hydraulic fracturing of the 3.5-km-deep Soultz geothermal well resulted in 200-fold permeability enhancement along an existing naturally conductive shear zone near the bottom of the well. The number of conductive fractures increased from about 20 to 100 after well stimulation. For tectonically active regions, Ingebritsen and Manning (2010) proposed that their permeability decay relationship be shifted by two orders of magnitude (Figure 1):

$$\log k = -3.2 \log z - 12. \qquad (2)$$

Estimates of crystalline basement fault and bulk permeability from hydrologic modeling studies of triggered seismicity consistently fall to the right of the Ingebritsen & Manning (1999) curve (Figure 1). Many of these study sites are located in the relatively stable North American craton, so that one might expect them to fall near that curve. We propose that permeability increases associated with water injection could explain this discrepancy.

Fault-zone architecture can potentially exert important controls on fluid flow. The permeability of fault-zone

architectural elements can vary by several orders of magnitude relative to the host rock, and fault zones can act both as flow conduits and flow barriers (Evans et al. 1997). Open fracture networks greatly increase host-rock permeability, whereas cataclasis and cementation in faults can greatly reduce permeability perpendicular to the fault plane (Caine et al. 1996). The key architectural elements are the fault core and bounding damage zone (Figure 2), both of which differ structurally and mechanically from the undeformed protolith (Caine et al. 1996; Knott et al. 1996; Kim et al. 2004). Grain-size reduction and/or mineral precipitation in the *fault core* generally yields lower permeability than undeformed protolith (Antonellini and Aydin 1994; Evans et al. 1997). The *damage zone* is the deformed volume surrounding the fault core and may contain fractures over a wide range of length scales, subsidiary faults, veins, stylolites, cleavage, deformation bands, and folds (Wibberley and Shimamoto 2002; Berg and Skar 2005; Faulkner et al. 2010). Damage zone structures in crystalline rocks tend to enhance fault zone
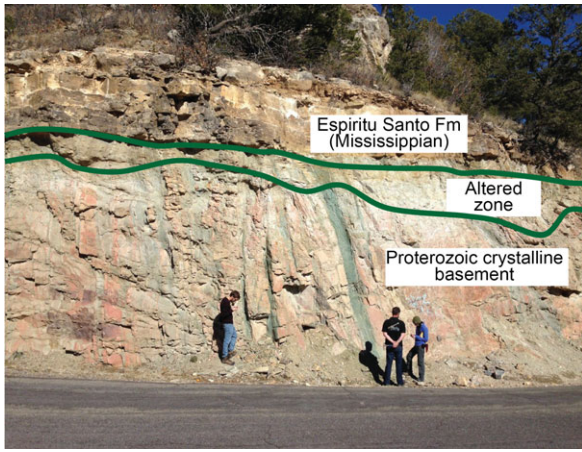
Figure 3. Field outcrop showing an altered zone located along a basal nonconformity in the Sangre de Cristo Mountains near Las Vegas, NM (adapted from Kerner et al. 2015).

permeability relative to both the core and the undeformed protolith, and the juxtaposition of these elements (Figure 2) creates major permeability contrasts within the fault zone (Goddard and Evans 1995; Caine et al. 1996; Wibberley and Shimamoto 2002). Damage zone permeability can be 2 to 3 orders of magnitude greater than the permeability of fractured protolith and four to six orders of magnitude greater than the fault core permeability (Caine et al. 1996). In some cases, however, core tests on granitic rocks reveal slightly higher core permeabilities relative to the protolith as confining pressure is increased (Evans et al. 1997). This is attributed to the smaller, more poorly connected fractures in the protolith closing more readily than the throughgoing fractures in the fault core. Anisotropic permeability structures are more influenced by the magnitude of permeability contrasts of the fault-zone elements than their absolute values (Caine et al. 1996; Evans et al. 1997). The conceptual model proposed by Caine et al. (1996) evaluates the permeability structure of fault zones by identifying a range of configurations of the three fault zone components: fault core, damage zone, and protolith. These architectural styles are conduits, barriers, and combined conduit-barriers.

The presence of low-permeability altered/weathered basement rocks along the sedimentary-basement nonconformity (Figure 3) has been proposed as a potentially mitigating factor for seismic risk (Figure 4; Kerner 2015). In the cases where nonconformities are seals they behave as confining layers (Zhang et al. 2013). At some field sites in New Mexico (Figure 3) and Colorado these zones exhibit granular flow deformation along a regional nonconformity separating Precambrian crystalline basement and late Devonian-Pennsylvanian sedimentary units. This zone along the nonconformity can be recognized as a distinct hydrogeologic unit due to its unique properties relative to the crystalline basement and overlying sedimentary layer.

In this study, we refer to this unit as the *altered zone* and assess the effects of its hydrologic properties

on downward pressure propagation. The unit may result from weathering and near-surface alteration prior to burial (Kerner 2015) or fluid-rock alteration after deposition, such as sericitization of feldspar (Cuccio 2017). Little is known about the occurrence, lateral continuity, and controls on such zones. In outcrop studies, thicknesses vary between 0 and 7 m over lateral distances of as little as 10 to 20 m, possibly as a function of pre-burial interface topography (Kerner 2015; Cuccio et al. 2016; Hesseltine et al. 2016; Cuccio 2017). A laterally discontinuous altered zone that pinches in and out has less ability to attenuate the downward migration of pore pressures than a laterally continuous zone. The absence of an altered basal seal was noted by Horton (2012) and Zhang et al. (2013) as a potential factor contributing to fluid migration along conductive basement faults near Guy, Arkansas.

Few models of fault-controlled induced seismicity explicitly take into account fault-zone architectural elements. Rinaldi et al. (2014) used a hydro-geomechanical model to assess seal failures resulting from CO_2 injection. They incrementally increased the damage zone thickness (5 to 45 m) and permeability and included brittle failure of protolith and damage zone in their coupled governing equations. The most important factors controlling seal breach and CO_2 leakage were hydraulic and mechanical properties of the damage zone (Rinaldi et al. 2014). Homogeneous, continuous damage zones with relatively high permeability (10^{-15} m^2) allowed seal breach. Reducing damage zone permeability by two orders of magnitude (to 10^{-17} m^2) resulted in CO_2 containment.

Zhang et al. (2013) considered a permeable, 2-m-wide, anisotropic Precambrian basement normal fault ($k_x = 10^{-15}$ m^2, $k_z = 10^{-13}$ m^2) with a proximal (25 m) basal reservoir injection well ($Q = 5455$ m^3/d). The failure envelope, which encompassed elevated pressures between 60 and 160 m head (0.6 and 1.6 MPa), extended to 4 km depth after 10 years. Zhang et al. (2016) considered fluid migration along a much wider (2 km) conductive ($k = 10^{-14}$ to 10^{-15} m^2) fault zone in their analysis of potential linkages between triggered seismicity (mean hypocenter depth ∼ 11 km) and oil field brine reinjection adjacent to the Dagger Draw oil field in the Permian basin, NM. In that study, elevated fluid pressures (greater than 7 m or 0.07 MPa) extended to depths of greater than 10 km after about 6 years of injection. While the 2 km width of that fault zone seems unrealistic, it is possible that hydraulic fracturing in the adjacent crystalline basement rocks increased the effective width of the damage zone. Here we extend this previous work by closely examining the impact of realistic fault zone permeability structures and low-permeability altered zones in facilitating or obstructing downward propagation of pore fluid pressures. Furthermore, we investigate a potential mechanism of deep, triggered seismic events by considering the possible role of pressure-driven permeability enhancement in promoting even deeper regions of elevated pore pressures.
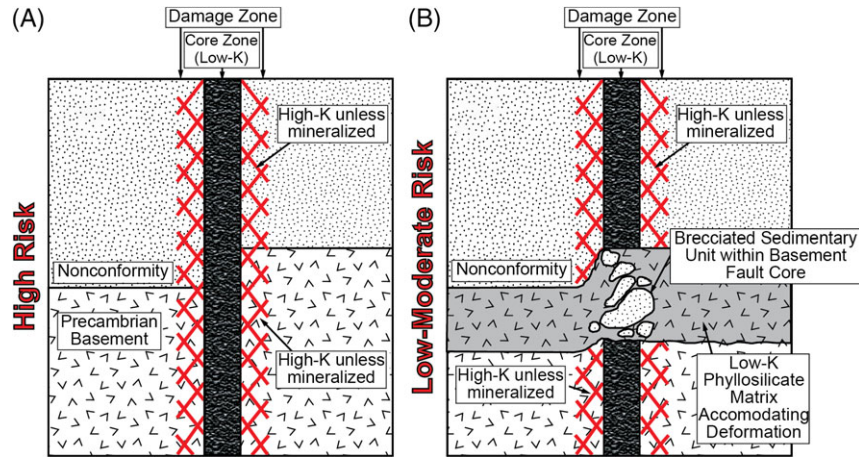
Figure 4. Conceptual diagrams showing relative risk of injection-induced seismicity given (A) lack of altered zone/basal seal and (B) presence of altered zone (gray) (adapted from Kerner 2015).

Research Methods

Groundwater Flow Equation

We use three-dimensional hydrogeologic models to assess fluid migration along crystalline basement faults using MODFLOW, a public domain groundwater flow model (Harbaugh and McDonald 1996; Harbaugh et al. 2000) that solves the following groundwater flow equation:

$$\frac{\partial}{\partial x}\left(K_x \frac{\partial h}{\partial x}\right) + \frac{\partial}{\partial y}\left(K_y \frac{\partial h}{\partial y}\right) + \frac{\partial}{\partial z}\left(K_z \frac{\partial h}{\partial z}\right)$$
$$= S_S \frac{\partial h}{\partial t} + Q(x, y, z, t) \qquad (3)$$

where h is the hydraulic head [L], K is the hydraulic conductivity tensor [L/T], S_s is the specific storage [L^{-1}], Q is the fluid injection source term (i.e., injection well) [T^{-1}], and t is time [T]. Equation 3 represents single-phase, constant-density groundwater flow in a three-dimensional, Cartesian coordinate system. Hydraulic conductivity is a lumped parameter that includes the influence of fluid and medium properties and is defined by $K = k\rho_f \ g/\mu$, where K is hydraulic conductivity, m/s; k is intrinsic permeability, m^2; ρ_f is fluid density, 997 kg m^{-3} (water); g is the acceleration due to gravity, 9.81 m s^{-2}; and μ is the dynamic viscosity of the fluid, 8.9×10^{-4} kg/m/s.

Solution Schemes, Boundary, and Initial Conditions

Three-Dimensional Model

Models were run for 19 years with a time step size of 2.5 h for 1 day, subsequently increasing to 30 days for the remainder of the 19 years. We used a constant injection rate of 5000 m^3/day (roughly 1000 gpm) in all simulations. This injection rate falls within the ranges used in other studies such as Keranen et al. (2014) near Jones, Oklahoma, where four high-rate wells had an injection rate of about 4 million barrels per month (~5300 m^3/d).

In all cases we placed the injection well within the basal reservoir 150 m from the fault zone except for one set of simulations in which we tested the effect of increasing well-fault distance to 1 and 2 km.

The model domain is 8 km by 8 km by 10 km (Figure 5) and includes 64 columns, 74 rows, and 25 vertical layers (x, y, and z dimensions, respectively; 126,750 nodes). We used localized grid refinement in order to more accurately resolve hydraulic head values near the fault zone, injection well, and the reservoir-basement interface. Horizontal grid discretization (Δx, Δy) was gradually increased from 10 to 630 m, with higher resolution close to the fault zone and increasing grid spacing toward the boundaries. Vertical discretization varied between 8 and 1000 m, with higher resolution near the reservoir-basement interface and increased spacing toward the base of the domain. We used the groundwater modeling software package Aquaveo™ GMS to build the grids and run the simulations.

The vertical fault zone in our models was varied between 30 and 150 m width. In all scenarios, the vertical fault zone extends to the bottom of the model domain. A scenario in which the fault terminates at the reservoir-basement nonconformity is referred to as a Proterozoic fault (Figure 6B). The scenario in which the fault cuts the reservoir (and altered zone, where present) in addition to the basement is termed a Paleozoic fault (Figure 6C to 6F). The uppermost (injection) horizon consists of two uniformly spaced layers totaling 80 m in thickness. The altered zone between the injection horizon and underlying crystalline basement (when included) is represented by five uniformly spaced layers between 1 and 20 m in total thickness. In one scenario, we represented a discontinuous (undulating) altered zone by discrete, 20-m-wide fault-parallel blocks such that the altered zone "pinches out" completely in evenly-spaced intervals (Figure 6D inset). The underlying crystalline basement comprises the remaining layers, which increase in thickness from 8 to 1000 m with depth away from the reservoir-basement interface.
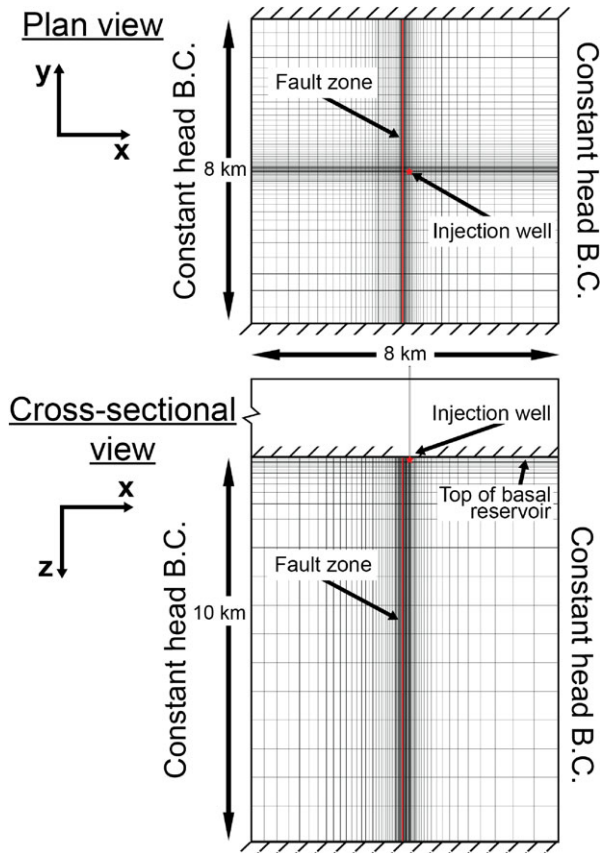
Figure 5. MODFLOW model domain grid discretization and boundary conditions presented in (top) plan view, and (bottom) cross-sectional view. No-flux boundary on top of model domain simulates a very tight (i.e., nonleaky) confining unit overlain by a thick (∼3 km) sequence of sedimentary rocks.

We imposed no-flux boundary conditions along the top and base of the model, as well as along the north and south lateral boundaries. The top of the model domain represents a basal reservoir overlain by a thick (∼3 km) sequence of sedimentary rocks. We assume that the reservoir is overlain by a very tight (i.e., nonleaky, $k < 10^{-19}$ m^2) confining unit such that there is no upward pore pressure leakage. We approximate this by imposing a no-flux boundary condition along the top surface. Constant head boundary conditions ($h = 10,000$ m) are enforced along the east and west lateral boundaries, and $h = 10,000$ m was also the initial head value for all cells. These lateral boundaries are far enough away from the injection well and fault zone, and the total simulation time sufficiently short, that simulated head increases were not significantly affected by these boundaries. In the simulations testing the effect of increased well-fault distance, we likewise placed the right lateral boundary 4 km from the well in keeping with our goal of minimizing boundary effects.

Two-Dimensional Dynamic Permeability Model

We also solved a two-dimensional (cross-sectional) form of Equation 3 for the dynamic permeability scenarios

using MATLAB. We used the Theis (1935) analytical solution to represent pressure buildup (s) at injection well nodes within the reservoir:

$$s = \frac{Q}{4\pi T} W(u) \qquad u = \frac{r^2 S}{4Tt}, \qquad (4)$$

where Q (m^3/d) is the injection rate of the well (positive), T is transmissivity (m^2/d), u is the argument of the well function $W(u)$ (Theis 1935), r (m) is the radial distance (here taken to be the radius of the injection well), S (dimensionless) is the storativity of the reservoir, and t (days) is time of injection. The well function is approximated by the infinite series:

$$W(u) = -0.577216 - \ln u + u - \frac{u^2}{2 \times 2!}$$

$$+ \frac{u^3}{3 \times 3!} + \cdots + \frac{u^{20}}{20 \times 20!} \qquad (5)$$

Permeability was allowed to increase when a threshold head was exceeded (5 m, 10 m), similar to the method specified in Rojstaczer et al. (2008). Their method increased permeability at a pressure threshold between 105% and 115% of hydrostatic; at 100 m depth, this threshold range corresponds to roughly 5.1 to 15.3 m excess hydraulic head. The underlying assumption is that ambient fluid pressures are near hydrostatic, and that in any volume of fractured rock there is some appropriately oriented fracture that will slip if the pressure increases by a sufficient amount; the latter assumption is reasonable for the western United States where rocks are critically stressed (Townend and Zoback 2000). Unlike the Rojstaczer et al. (2008) model, permeability does not decrease with time. We employ a modified version of the predictor–corrector iterative method in order to address the nonlinearity introduced by large permeability enhancements (50%) during a single time step. In our implicit finite-difference formulation, we make an initial estimate of head at the next time step ($\widehat{h}_{t+1}$). Permeability at this advanced time step ($\widehat{k}_{t+1}$) is increased for all cells with estimated heads exceeding the prescribed threshold. We then calculate permeability in the middle of the time step by taking the arithmetic average of the present and future time steps ($k_{t+1/2} = (k_t + \widehat{k}_{t+1})/2$). We use this time-averaged permeability ($k_{t+1/2}$) to make an improved calculation of head at the next time level (h_{t+1}). We used the Gauss–Seidel method to calculate head changes.

Due to the added computational costs of these dynamic permeability simulations, we constrained the dimensions of the model domain to a cross section 250 m wide and 10,000 m deep. Computational limitations associated with MATLAB prevented us from running these models longer than 10 days; however, we were able to run the models with static permeability and larger time steps for 4 years, closely approximating the overall propagation depth of the 2-m head contour and well-head pressure of the three-dimensional model, giving us some confidence in the shorter dynamic permeability simulations.
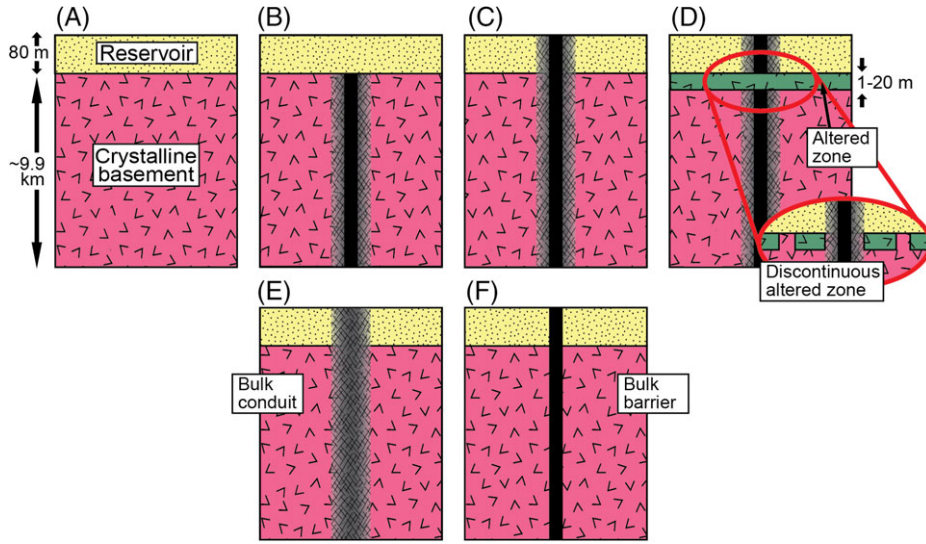
Figure 6. Hydrogeologic framework used in sensitivity analysis (not to scale): (A) Unfaulted case, (B) Proterozoic conduit-barrier fault; (C) Paleozoic conduit-barrier fault; (D) Paleozoic conduit-barrier fault with a laterally continuous altered zone as a basal seal and also showing (inset) a discontinuous or undulating altered zone; and permeability architecture end-members: (E) conduit fault zone, and (F) barrier fault zone. Note that top of the model domain is intended to represent a confined basal reservoir overlain by thick (~3 km) sequence of sedimentary rocks (not shown).

Wellhead pressure changes were represented using the Theis solution (4) calculated based on a constant rate of injection (5000 m³/d) for 10 days with time steps of 0.01 days (~14 min). These pressure changes were specified at two nodes in the reservoir on the right side of the domain located 150 m from the fault zone. We acknowledge that the radial Theis solution applied to a cross-section model is only an approximation of the actual conditions. Imposing Theis head changes at injection nodes is an ad-hoc way of representing injection; if we had assigned the Theis solution to all nodes in the reservoir, we would be imposing heads that assume no leakage in the reservoir, which would be incorrect. These are illustrative, idealized models against which we are not trying to match a particular field situation.

The grid discretization is uniform (i.e., nontelescoping). We used a horizontal discretization (Δx) of 5 m and vertical discretization (Δz) of 10 m. The injection reservoir was specified as the top 80 m of the domain and the underlying crystalline basement comprised the remainder. The fault zone was comprised of a fault core 10 m wide and equally-sized damage zone on either side.

We imposed a no-flux boundary on the top and bottom of the domain. We imposed a constant head boundary condition (0 m excess head) along the lateral boundaries with the exception of the reservoir injection nodes that had heads prescribed by the Theis solution. An initial condition of $h = 0$ m excess head was used in all model runs.

Hydrogeologic Framework for Sensitivity Studies

Both the three- and two-dimensional models are characterized by a relatively thin (80-m thick) sedimentary layer, into which fluid is injected (injection reservoir), overlying thick ($\geq$ 9.9 km) crystalline basement. In some cases, a very thin (1 to 20 m) altered zone at the reservoir-basement interface serves as an aquitard. A vertical, planar fault cuts the model domain in half and spans its width; its thickness and vertical extent are variable.

We consider a range of permeabilities for the altered zone and individual fault-zone components (Table 2). The fault is assumed to be either: (a) not present, (b) a Proterozoic fault hosted solely in the crystalline basement, or (c) a Paleozoic fault hosted in the basement and cutting the injection reservoir and altered zone (where present). Throw on the fault is assumed to be negligible. The fault is represented as one of three fault-zone archetypes: (1) conduit, characterized by elevated permeability compared to the undeformed host rock; (2) barrier, represented by reduced permeability; and (3) conduit-barrier, comprising a core region of low permeability surrounded by the highly permeable damage zone. In the first two cases, the permeability across the fault zone is homogeneous; the conduit-barrier case is represented by a single low-permeability central cell with high-permeability cells on either side. Cell permeabilities are generally treated as isotropic in this study, with the exception of one simulation (run 5 in Table 2) which produces a conduit-barrier fault zone by assigning anisotropy. For calculating effective anisotropy of the conduit-barrier fault zones, we use averaging equations for the effective permeability normal and parallel to the fault (x-axis, z-axis, respectively):

$$\widehat{k}_\perp = \frac{b_T}{\sum_{i=1}^{n} \frac{b_i}{k_i}} \qquad \widehat{k}_\parallel = \frac{\sum_{i=1}^{n} b_i k_i}{b_T}, \qquad (6)$$

where $\widehat{k}$ is effective permeability for either the fault-orthogonal ($\widehat{k}_\perp$) or fault-parallel ($\widehat{k}_\parallel$) direction, b is the

Table 2
Permeability (m^2) Values Varied in Sensitivity Study

Model Run	Altered zone k	Fault age	Fault Perm. Structure	Damage Zone k (res., a.z., bsmt.)	Core k (res., a.z., bsmt.)	Bulk Fault Zone Perm. (k_x, k_z)	Figure
1	—	—	—	—	—	—	7,8A
2	—	Prot.	conduit-barrier	— — 3×10^{-14}	— — 3×10^{-16}	—	7,8B
3	—	Pz	conduit-barrier	3×10^{-10} — 3×10^{-14}	3×10^{-16} — 3×10^{-16}	—	7,8C
4	—	Pz	barrier	—	—	3×10^{-18} 3×10^{-18}	7,8D
5	—	Pz	conduit-barrier	—	—	3×10^{-15} 3×10^{-13}	7E
6	—	Pz	conduit	—	—	3×10^{-14} 3×10^{-14}	7F (dashed), 8E
7	—	Pz	conduit	—	—	3×10^{-14} 3×10^{-14}	7F (contoured), 8F
8	3×10^{-18}	Pz	conduit-barrier	3×10^{-10} 3×10^{-18} 3×10^{-14}	3×10^{-16} 3×10^{-19} 3×10^{-16}	—	10B,C

a.z., altered zone; bsmt., basement; k, permeability; Prot., Proterozoic; Pz, Paleozoic; res., injection reservoir.

fault element width, n is the number of fault elements (2, in our case), and subscript i refers to the respective fault element. For flow parallel to the fault plane ($\widehat{k}_{||}$), the effective permeability is controlled by the higher-permeability damage zone. For flow perpendicular to the fault plane, the low-permeability core has a controlling effect.

Results

Effect of Fault–Zone Architecture

For our three-dimensional sensitivity study we first consider the effects of conduit-barrier Proterozoic and Paleozoic fault zones that include core and damage zones (runs 1 to 3 in Table 2). The crystalline basement permeability in all scenarios is 3×10^{-17} m^2 (Evans et al. 1997; Manning and Ingebritsen 1999). The vertical (Figure 7) and horizontal (Figure 8) patterns of excess pore pressure propagation are strongly controlled by fault zone properties (Table 2). None of these scenarios consider a laterally extensive, low-permeability altered zone; the 80-m-thick injection horizon rests directly on crystalline basement rock. Absent a fault zone, the 2-m head (0.02 MPa) envelope extends to approximately 600 m depth, diffusing roughly 500 m into the crystalline basement rock (Figure 7A). The deepest penetration of excess heads occurs directly under the injection well. Introducing a 30-m-wide Proterozoic conduit-barrier fault zone (i.e., basement fault terminates at the basement–reservoir interface) extends the 2-m head change envelope to depths of approximately 2500 m. A Paleozoic conduit-barrier fault (i.e., basement fault extending into reservoir rock) produced an excess pore pressure envelope extending to depths of approximately 2300 m (Figure 7C) with significant flow compartmentalization in the injection horizon (Figures 7C and 8C).

Elevated pore pressures on the order of 38 m head occur in proximity to the well (within a radius $r = 50$ m) versus only 22 m for the Proterozoic fault (Figure 7B).

In other simulations the fault zone was simply assigned bulk properties rather than subdivided into core and damage zone (Figures 7D to 7F and 8D to 8F). We considered a barrier fault zone end member by assigning isotropic permeability 4 orders of magnitude lower than the reservoir rock and 1 order of magnitude lower than the crystalline basement protolith ($k = 3 \times 10^{-18}$ m^2; Figures 7D and 8D). Elevated pore fluid pressures (≥ 20 m head; 0.2 MPa) built up primarily within the injection reservoir and were highly compartmentalized by the fault (Figures 7D and 8D). Pore pressures diffused into the basement to depths less than 700 m. We also computed excess heads for a 30-m-wide conduit-barrier fault zone (Figure 7E) represented using bulk anisotropic permeability with k_z 2 orders of magnitude greater than k_x; in this case, excess heads were mapped to a depth of approximately 4.2 km. When we treated the fault zone as a pure conduit (isotropic k set to 2 orders of magnitude greater than the host rock), widening the fault zone by a factor of 5 (to 150 m) increased the excess pressure propagation depth from approximately 2300 m (dashed, Figure 7F) to greater than 5300 m (contours, Figure 7F). Pressure was unevenly distributed across the reservoir fault zone despite the lack of a horizontal flow barrier (Figure 8F).

For one simulation (run 3 in Table 2) of a Paleozoic conduit-barrier fault, we tested the effect of injection at greater distances from the fault zone (Figure 9). When the injection well was 2 km from the fault (Figure 9C), there was significant reduction in downward pore pressure propagation (~900 m) due to radial dissipation of excess pressure.
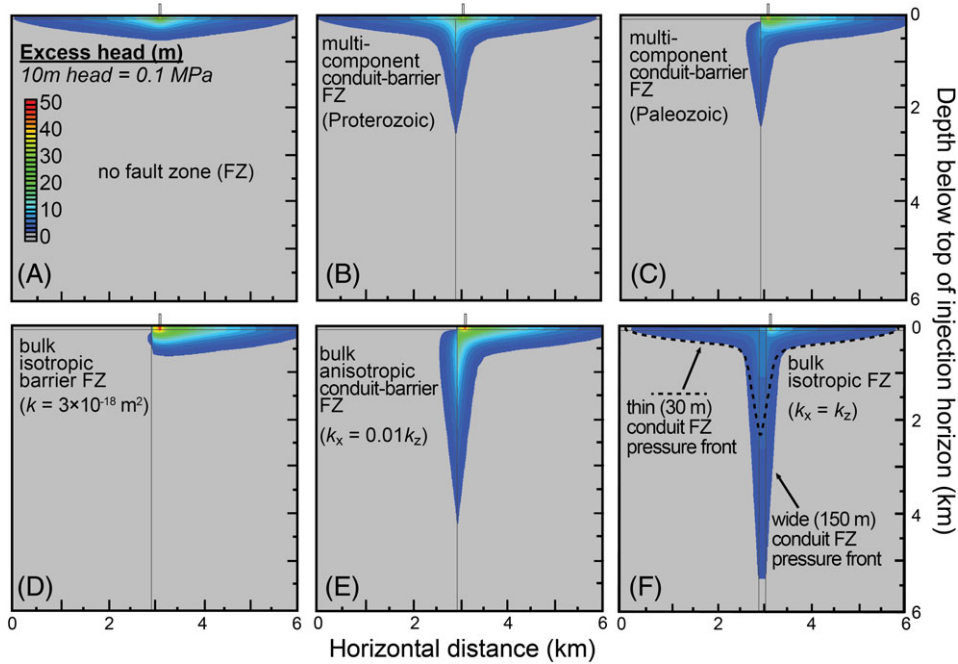
Figure 7. Cross-sectional views of pore pressure envelope propagation after 4 years of constant-rate injection with no altered zone. Simulations presented are: (A) unfaulted (B) Proterozoic conduit-barrier fault zone (C) Paleozoic conduit-barrier fault zone, (D) Paleozoic barrier fault zone assigned bulk isotropic properties ($k_x = k_z = 3 \times 10^{-18}$ m^2), (E) Paleozoic conduit-barrier fault zone assigned bulk anisotropic permeabilities (basement $k_x = 3 \times 10^{-15}$ m^2, $k_z = 3 \times 10^{-13}$ m^2), and (F) Paleozoic conduit fault zones assigned bulk isotropic permeabilities (basement $k_x = k_z = 3 \times 10^{-14}$ m^2), both for a thin (30-m-wide) fault zone (dashed line) and a thick (150-m-wide) fault zone. Vertical gray lines indicate location of the fault zone, and horizontal gray line denotes the reservoir-basement interface. Injection takes place 150 m to the right of the fault zone within the reservoir (well location indicated).
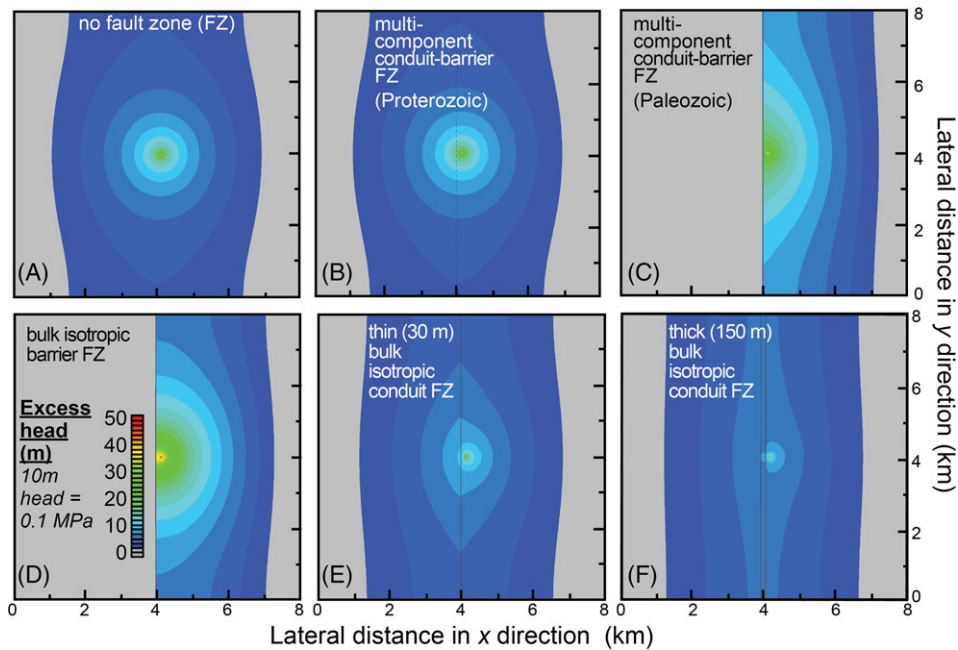

Figure 8. Plan view of pore pressures within the injection reservoir layer after 4 years of constant-rate injection with no altered zone and (A) no fault zone, (B) Proterozoic conduit-barrier fault zone, (C) Paleozoic conduit-barrier fault zone, (D) Paleozoic barrier fault zone assigned bulk isotropic properties ($k_x = k_z = 3 \times 10^{-18}$ m^2), (E) thin (30-m-wide) Paleozoic conduit fault zone, and (F) wide (150 m) Paleozoic conduit fault zone. Both conduit fault zones were assigned isotropic permeabilities (basement FZ $k_x = k_z = 3 \times 10^{-14}$ m^2). Injection takes place 150 m to the right of the fault zone.
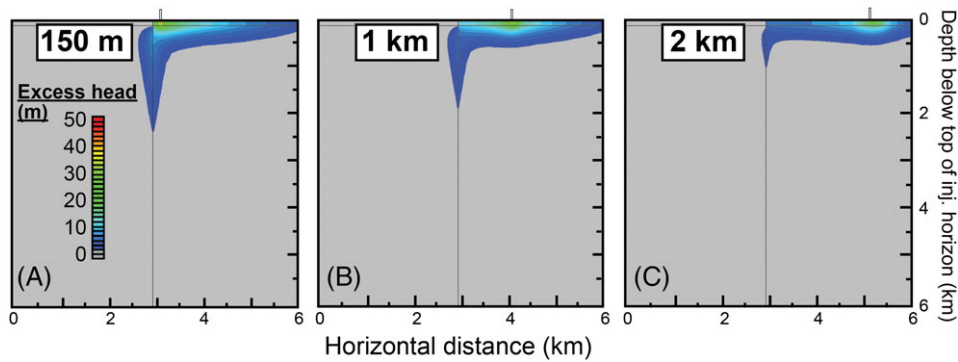
Figure 9. Effects of variable injection well distance from a Paleozoic conduit-barrier fault zone. Well distances (A) 150 m (identical to Figure 7C), (B) 1 km, and (C) 2 km. Injection well location is indicated on top of each panel. Transition from gray to dark blue contour denotes a 2-m increase in hydraulic head (0.02 MPa).
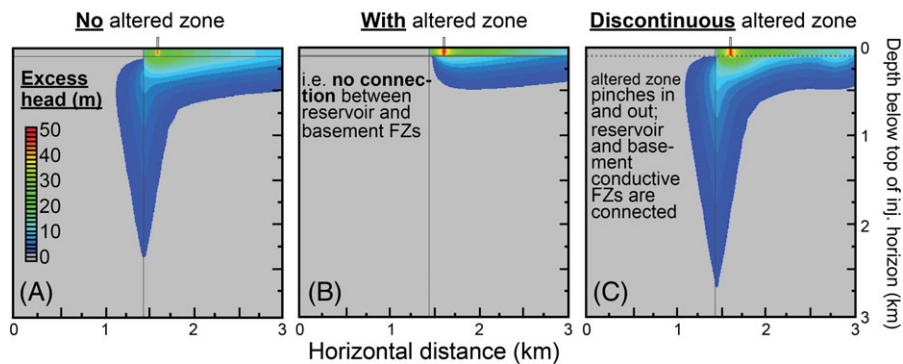
Figure 10. Excess heads after 4 years of constant-rate injection for a Paleozoic conduit-barrier fault scenario (A) absent an altered zone (identical to Figure 7C), (B) with an altered zone present as a continuous 20-m-thick confining layer, and (C) with a discontinuous altered zone that pinches in and out in 20-m horizontal intervals but reservoir and basement fault zones fully connected (similar to Figure 6D inset). Transition from gray to dark blue contour (and all subsequent contour lines) denotes a 2-m increase in hydraulic head (0.02 MPa).

Effect of Altered Zone

Because laterally continuous altered zones occur at some outcrop analogs to modern basal reservoir injection sites (Figure 3), we added a 20-m-thick, low-permeability $(k_x = k_z = 3 \times 10^{-18}$ m^2) altered zone (Figure 10B) to a Paleozoic conduit-barrier fault with properties identical to those presented in Figure 7C. The continuous altered zone suppresses downward pressure propagation (compare Figure 10A and 10B).

We also represented a spatially heterogeneous altered zone that pinches and swells discretely in 20-m-wide intervals (similar to the conceptual diagram in Figure 6D, inset) in order to test the effect of a laterally discontinuous confining layer. The fault zone in this scenario was not blocked by the altered zone. Elevated pore pressures propagated downward to depths of 2.7 km (Figure 10C) after 4 years of continuous injection.

Effect of Dynamic Permeability

We performed a sensitivity analysis using our MAT-LAB based cross-section model testing the effects of dynamic (i.e., pressure-enhanced) permeability increases on the pore-pressure envelope migration (Figure 11). We varied the differential excess pressure threshold required for permeability enhancement and the hydrogeologic

units in which permeability was allowed to increase. Injection reservoir permeability was not allowed to increase for any scenario. The results are compared to the static permeability case (Figure 11A), in which the 2-m hydraulic head contour propagated to a depth of approximately 1.9 km. When we allow a 50% permeability enhancement per 5-m excess head (0.05 MPa) to occur within the core, damage zone, and crystalline basement, the 2-m pore pressure contour extends to 3.5 km depth (Figure 11B). Permeability is enhanced within the core to the point that elevated pore pressures bleed over the left side of the fault. Permeability is enhanced to the prescribed maximum (2 orders of magnitude increase) within the damage zone flow conduit and also within the basement rock down to depths of approximately 1.4 km. When we restrict dynamic permeability enhancement to the damage zone and apply the same permeability enhancement criteria, we see focused propagation of fluid pressures, with the 2-m head contour extending to roughly the same depth (~3470 m) below the injection horizon (Figure 11C). For similar conditions, with the exception of increasing the excess head threshold to enhance permeability from 5 to 10 m (Figure 11D), we observe reduced migration depth of the pore pressure
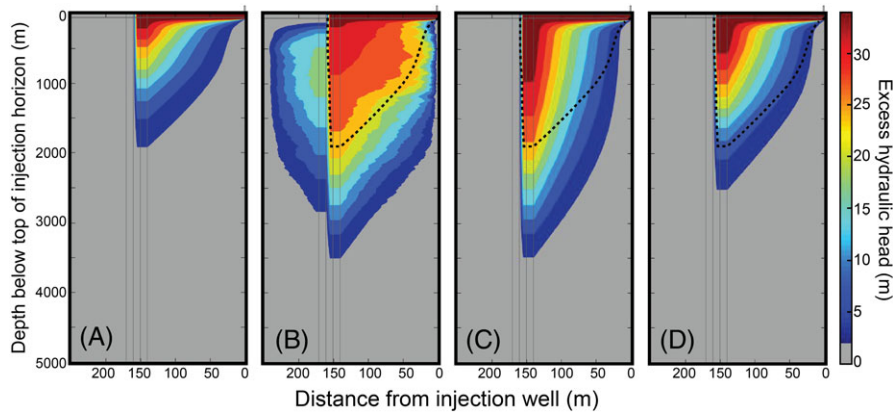
Figure 11. Simulations testing the effect of pressure-controlled dynamic permeability enhancement on pore pressure envelope migration depth along a Paleozoic conduit-barrier fault (vertical gray lines delineate central core and damage zone) after 10 days of pumping. The following scenarios were tested: (A) static permeability, (B) 5-m head threshold enhancing permeability step-wise by 50%, with permeability allowed to increase everywhere except the injection reservoir, (C) 5-m pressure threshold enhancing permeability step-wise by 50%, with permeability allowed to increase only in the fault damage zone, (D) 10-m pressure threshold enhancing permeability step-wise by 50%, where permeability can only increase in the damage zone. Dotted line shows the extent of the static permeability result in A for comparison. Results shown for the top 5 km of the model domain with 10× horizontal exaggeration. Injection well location is indicated on top of each panel.

envelope (2.5 km), though still increased from the static permeability scenario (1.9 km; Figure 11A).

Discussion

When we assume no fault zone or low-permeability altered zone is present and invoke representative injection-reservoir and crystalline-basement permeabilities (3×10^{-17} m^2), the buildup of elevated pore pressures within the basement extends to depths of less than 600 m (Figure 7A) after 4 years of constant injection into the basal reservoir. Such conditions may be similar to the case of induced seismicity in Youngstown, Ohio (Kim 2013), and not all injection-induced earthquakes are necessarily caused by pressure migration along conductive fault zones. It is clear, however, that in the scenarios we considered, some other feature must be present to allow propagation of elevated pore pressures to crystalline basement depths of 2–10 km (Zhang et al. 2016) where we expect large, damaging induced earthquakes. Two main possibilities exist: either the bulk permeability of the crystalline basement is higher than previous work suggests, or the injected fluids encounter a high-permeability fault and/or fracture zone(s). Several fault-zone architectures allow elevated pore fluid pressures to penetrate to significant depths within the crystalline basement rock.

Conduit-barrier fault zones represented by high-permeability damage zones and lower-permeability cores were effective in transmitting fluids to depths of 2.3–2.5 km (Figure 7B and 7C), similar to the depths of triggered seismicity observed in Guy, Arkansas (Horton 2012). A Paleozoic fault zone was able to compartmentalize flow within the reservoir (Figure 8C) due to its low-k core, while also promoting preferential downward flow along the higher-k damage zone (Figure 7C), despite damage-zone permeability an order of magnitude less than that of the injection reservoir.

This study used a very high-rate injection well ($Q = 5000$ m^3/d) in the nearby vicinity of a fault zone (150 m). Wellhead pressures are directly proportional to the injection rates. While high, this injection rate is consistent with the injection rates in other hydrogeologic models of induced seismicity (Zhang et al. 2013, 2016; Keranen et al. 2014). Furthermore, we invoked a single well, whereas wastewater disposal areas may have well densities greater than 1 km^{-2}. Injection in the Illinois Basin found that injection at adjacent wells leads to overlapping envelopes of increased pressure (Bandilla et al. 2013). Pressure response is magnified by pressure change interference patterns resulting from the interaction of multiple injection sites. Multiple adjacent wells injecting fluid at lower rates could also produce elevated pressures similar to those in the present study.

We performed two simulations of wells injecting at greater distances of 1 km (Figure 9B) and 2 km (Figure 9C) from a Paleozoic conduit-barrier fault zone. Increasing the well distance to 1 km reduced the propagation depth of the pore pressure envelope to 1.9 km (Figure 9B), significantly larger than the unfaulted scenario that did not result in elevated pressures below 600 m (Figure 9A). Increasing the well distance to 2 km from the fault zone caused the excess pore pressure envelope to migrate to only approximately 900 m depth within the basement (Figure 9C).

Representing the conduit-barrier fault zone by multiple architectural elements with highly contrasting, isotropic permeabilities ($k_{\text{damage zone}} = 100 \times k_{\text{core}}$) hindered flow across the fault plane and promoted flow parallel to the fault plane (Figure 7C). Overall patterns closely approximated those of the simulation with a bulk anisotropic fault zone ($k_{\parallel} = 100 \times k_{\perp}$; Figure 7E), but with shallower depths of penetration. By averaging the fault permeability properties (Equation 6), we determine

that the individual fault zone architectural elements create an effective permeability anisotropy in the basement fault zone whereby the ratio of orthogonal to parallel fault zone permeability ($k_\perp/k_\parallel$) was 0.04, whereas for the simulation with assigned anisotropy this ratio was 0.01. This is consistent with the observed shallower depths of pressure propagation for the fault zone represented by individual architectural elements.

Although realistic fault-zone architectural elements and permeabilities in our model effectively transmitted elevated pore pressures to depths of about 2.5 km, we are unable to explain much deeper (greater than 10 km depth) instances of seismicity (Zhang et al. 2016) without introducing a wide or very high-permeability fault zone (Figure 7F). We examined pressure-induced dynamic permeability enhancement as one possible way to increase pressure transmission in a multi-component conduit-barrier fault zone (Figure 11). Our dynamic permeability simulations ran for only 10 days rather than 4 years, as in the three-dimensional model, because of computational costs. Dynamic permeability enhancement expands the pore pressure increase envelope relative to the static permeability simulation (Figure 11A). The geometry and extent of expansion depends on which hydrogeologic units undergo permeability enhancement, and on the enhancement parameters (e.g., the excess pressure threshold required to trigger enhancement). Great increases in penetration depth occurred when pressure thresholds were low (5 m excess hydraulic head, or 0.05 MPa; Figure 11B and 11C). Dynamic permeability enhancement over 10 days extended the pressure front migration depth to from 1.9 km to 3.5 km in these scenarios.

We present such models as idealized proof-of-concept simulations. For the dynamic permeability scenarios, we used an arbitrary but representative overall maximum magnitude (100-fold) of permeability increase (Evans et al. 2005). We did not formally couple groundwater flow with geomechanical deformation, nor did we consider changes in shear or normal stress in calculating failure (Rutqvist et al. 2016). It is worth noting that permeability enhancement in the field is not aseismic—fracture stimulation is generally accompanied by microseismicity caused by very small shear dislocations (Evans et al., 2005). However, most seismic networks are not nearly dense enough to detect this level of microseismicity, and quantitative insight into the resulting changes in fracture permeability can only be accurately determined within or very close to the borehole. It is therefore not always clear whether permeability enhancement will occur based on pressure alone; critically stressed faults/fractures do not occur everywhere and not all are well connected – our model assumes both are true.

Evans et al. (2005) showed that massive fluid injections into relatively low-permeability crystalline basement rock ($\sim 10^{-17}$ m^2) focused 95% of the flow at just 10 discrete fractures. The resultant permeability enhancement occurred primarily within these preexisting fractures while also creating local, newly permeable fractures. Our model restricting permeability stimulation to the fractured

damage zone is analogous. Permeability enhancement in the fault core is less likely because there is often a high degree of alteration that reduces the likelihood of brittle failure (Kerner 2015). Hydrothermal alteration, which is commonly present in granite fault cores (Evans et al. 2005), tends to suppress dilation from shear dislocations (Sausse 2002). Illite present in altered crystalline fault core can also clog pores and microcracks (Evans et al. 2005; Sausse and Genter 2005).

Several recent triggered earthquake sequences can potentially be explained by conductive fault zones and/or dynamic permeability. Hornbach et al. (2015) attributed a series of deep earthquakes (up to 5 km below the injection interval) in the Fort Worth Basin in 2013 to downward pressure propagation within a fault system. Assuming very low (10^{-19} m^2) granite permeability, they posited preferential flow along higher permeability damage zone conduits parallel to the fault. The injector wells in their study were roughly 2 km away from the fault zone.

Conductive fault zones may have also played a role in the 2014 triggered seismic sequence in Milan, KS. Choy et al. (2016) calculated bulk hydrologic diffusivity between 0.3 and 2.0 m s^{-2} ($k \sim 3 \times 10^{-14}$ and 2×10^{-13} m^2) to explain a large mainshock occurring 3.5 km below the injection interval of wells located 4−8 km away, 5 months after a rapid increase in injection rates. Such permeabilities are quite probable within the Arbuckle Formation and the uppermost basement; however, an alternative scenario is similar to that presented in Figure 9B, wherein pressures propagate horizontally within the injection reservoir and then downward parallel to the fault plane.

The Fairview, OK triggered earthquake sequence in early 2016 (Yeck et al. 2016) is a possible example of hydraulic fracturing owing to far-field pressurization. This sequence exhibited diffuse seismicity near the clustered highest-rate wastewater injection wells. The majority of large seismic events occurred 12+ km to the southwest, along part of a 14-km-long fault segment. While the authors posit that the permeable ($k \sim 1 \times 10^{-12}$ m^2) Arbuckle injection horizon could have transmitted elevated pressures reflecting a sevenfold increase in injection rates from mid-2014 to mid/late-2015, preferential flow paths along conductive fault zones might also have served to propagate increases in fluid pressure. Yeck et al. (2016) ruled out any impact from sporadic daily variation in well operations, calculating that this would require permeability between 2.5×10^{-11} and 3.5×10^{-10} m^2, roughly 1−3 orders of magnitude greater than the largest permeabilities observed in previous cases of induced seismicity. However, hydraulic stimulation could possibly have served to increase permeability to this degree, allowing short-term variations in well injection rates to play a role in seismicity.

Some of our simulations depicted a thin, laterally continuous altered zone at the reservoir-basement interface, and confirmed our hypothesis that such a unit could significantly reduce the depth of pore pressure front propagation (less than 500 m) into the basement, even

in the presence of a conductive fault zone (Figure 10B). Field observations in New Mexico and Colorado by Kerner (2015) suggest that reduced permeability is caused by surficial weathering pre-burial and circulation of hydrothermal fluids post-burial. The fault zone in the altered layer typically remains unfractured due to the semi-ductile behavior of its phyllosilicate matrix (Kerner 2015); for this reason, conduit and conduit-barrier fault zones generally do not communicate through the altered zone (Figure 10B). However, ongoing fieldwork reveals, in some locations, spatially heterogeneous altered zones that pinch and swell along the nonconformity, reducing its overall ability to inhibit pressure transmission.

Conclusions

Conductive fault zones represented by realistic permeability architecture are a viable mechanism for transmitting elevated fluid pressures from a basal injection horizon to considerable depths (∼2.5 km) within crystalline basement rock. We hypothesize dynamic permeability enhancement caused by excess pressures to be a potential mechanism for triggering deeper induced events (6–10 km) and confirm that this process can greatly increase the depth of pressure front propagation. We also note the effectiveness of even a thin (5–20 m), laterally continuous altered zone at the reservoir-basement interface in hindering the downward propagation of elevated pore pressures that could otherwise be transmitted by conductive faults. However, more field and core log observations are needed to confirm both the existence and lateral continuity of this distinct hydrogeologic unit.

Acknowledgments

References

Antonellini, M., and A. Aydin. 1995. Effect of faulting on fluid flow in porous sandstones: Geometry and spatial distribution. *AAPG Bulletin* 79: 642–670.

Antonellini, M., and A. Aydin. 1994. Effect of faulting on fluid flow in porous sandstones: Petrophysical properties. *AAPG Bulletin* 78, no. 3: 355–377. https://doi.org/10.1306/8D2B1B60-171E-11D7-8645000102C1865D

Bandilla, K.W., M.A. Celia, T.R. Elliot, M.A. Person, K.M. Ellett, J.A. Rupp, C.W. Gable, and Y. Zhang. 2013. Modeling carbon sequestration in the Illinois Basin using a vertically-integrated approach. *Computing and Visualization in Science* 2012: 39–51. https://doi.org/10.1007/s00791-013-0195-2

Bense, V.F., and M.A. Person. 2006. Faults as conduit-barrier systems to fluid flow in siliciclastic sedimentary aquifers.

Water Resources Research 42, no. August 2005: 1–18. https://doi.org/10.1029/2005WR004480

Berg, S.S., and T. Skar. 2005. Controls on damage zone asymmetry of a normal fault zone: Outcrop analyses of a segment of the Moab fault, SE Utah. *Journal of Structural Geology* 27, no. 10: 1803–1822. https://doi.org/10.1016/j.jsg.2005.04.012

Caine, J.S., J.P. Evans, and C.B. Forster. 1996. Fault zone architecture and permeability structure. *Geology* 24, no. 11: 1025–1028. https://doi.org/10.1130/0091-7613(1996)024<1025

Choy, G.L., J.L. Rubinstein, W.L. Yeck, E. Daniel, C.S. Mueller, and O.S. Boyd. 2016. A rare moderate-sized (M w 4.9) Earthquake in Kansas: Rupture process of the Milan, Kansas, Earthquake of 12 november 2014 and its relationship to fluid injection. *Seismological Research Letters* 87, no. 6: 1433–1441. https://doi.org/10.1785/0220160100

Cuccio, L. 2017. *Geological Characterization of Precambrian Nonconformities: Implications for Injection- Induced Seismicity in the Midcontinent United States*. Logan, Utah: Utah State University.

Cuccio, L. A., J. P. Evans, K. K. Bradbury, and P. S. Mozley. 2016. Hydrological analysis of nonconformities: Implications for injection-induced seismicity in the midcontinent United States. In *GSA Annual Meeting* (p. 2016). https://doi.org/10.1130/abs/2016AM

Evans, K.F., A. Genter, and J. Sausse. 2005. Permeability creation and damage due to massive fluid injections into granite at 3.5 km at Soultz: 1. Borehole observations. *Journal of Geophysical Research* 110, no. 4: 1–19. https://doi.org/10.1029/2004JB003169

Evans, J.P., C.B. Forster, and J.V. Goddard. 1997. Permeability of fault-related rocks, and implications for hydraulic structure of fault zones. *Journal of Structural Geology* 19, no. 11: 1393–1404. https://doi.org/10.1016/S0191-8141(97)00057-6

Faulkner, D.R., C.A.L. Jackson, R.J. Lunn, R.W. Schlische, Z.K. Shipton, C.A.J. Wibberley, and M.O. Withjack. 2010. A review of recent developments concerning the structure, mechanics and fluid flow properties of fault zones. *Journal of Structural Geology* 32, no. 11: 1557–1575. https://doi.org/10.1016/j.jsg.2010.06.009

Forster, C.B., and J.P. Evans. 1991. Hydrogeology of thrust faults and crystalline thrust sheets: Results of combined field and modeling studies. *Geophysical* 18, no. 5: 979–982.

Goddard, J.V., and J.P. Evans. 1995. Chemical changes and fluid-rock interaction in faults of crystalline thrust sheets, northwestern Wyoming, U.S.A. *Journal of Structural Geology* 17, no. 4: 533–547. https://doi.org/10.1016/0191-8141(94)00068-B

Harbaugh, A. W., E. R. Banta, M. C. Hill, and M. G. McDonald. 2000. MODFLOW-2000, The U.S. Geological Survey modular ground-water model — User guide to modularization concepts and the ground-water flow process. U.S. Geological Survey. http://www.gama-geo.hu/kb/download/ofr00-92.pdf

Harbaugh, A. W., and M. G. McDonald. 1996. User's Documentation for MODFLOW-96, an update to the U.S. Geological Survey Modular Finite-Difference Ground-Water Flow Model. *U.S. Geological Survey Open File Report*, 96 (485).

Hesseltine, G., J. P. Evans, K. R. Kerner, and P. S. Mozley. 2016. Structural diagenesis and micro- to macro-scale structural architecture of basal nonconformities. In *GSA Annual Meeting*. https://doi.org/10.1130/abs/2016AM

Hornbach, M.J., H.R. Deshon, W.L. Ellsworth, B.W. Stump, C. Hayward, C. Frohlich, H.R. Oldham, J.E. Olson, M.B. Magnani, C. Brokaw, and J.H. Luetgert. 2015. Causal factors for seismicity near Azle, Texas. *Nature Communications*: 1–11. https://doi.org/10.1038/ncomms7728

Horton, S. 2012. Disposal of Hydrofracking waste fluid by injection into subsurface aquifers triggers earthquake swarm in Central Arkansas with potential for damaging earthquake. *Seismological Research Letters* 83, no. 2: 250–260. https://doi.org/10.1785/gssrl.83.2.250

Hsieh, P.A., and J.D. Bredehoeft. 1981. A reservoir analysis of the Denver earthquakes: A case of induced seismicity. *Journal of Geophysical Research* 86: 903–920. https://doi.org/10.1029/JB086iB02p00903

Ingebritsen, S.E., and C.E. Manning. 2010. Permeability of the continental crust: Dynamic variations inferred from seismicity and metamorphism. *Geofluids* 10: 193–205. https://doi.org/10.1111/j.1468-8123.2010.00278.x

Ingebritsen, S.E., and C.E. Manning. 1999. Geological implications of a permeability-depth curve for the continental crust. *Geology* 27, no. 12: 1107–1110.

Keranen, K.M., M. Weingarten, G.A. Abers, B.A. Bekins, and S. Ge. 2014. Sharp increase in Central Oklahoma seismicity since 2008 induced by massive wastewater injection. *Science* 10, no. 1126: 448–451. https://doi.org/10.1038/45144

Keranen, K.M., H.M. Savage, G.A. Abers, and E.S. Cochran. 2013. Potentially induced earthquakes in Oklahoma, USA: Links between wastewater injection and the 2011 Mw 5.7 earthquake sequence. *Geology* 41, no. 6: 699–702. https://doi.org/10.1130/G34045.1

Kerner, K.R. 2015. *Permeability Architecture of Faulted Nonconformities: Implications for Induced Seismicity*. Socorro, New Mexico: New Mexico Institute of Mining and Technology.

Kerner, K. R., P. S. Mozley, J. P. Evans, and M. A. Person. 2015. Geologic Controls on Injection Related Reactivation of Basement Faults. In *AAPG Annual Convention and Exhibition*.

Kim, W. 2013. Induced seismicity associated with fluid injection into a deep well in Youngstown, Ohio. *Journal of Geophysical Research. Solid Earth* 118: 13. https://doi.org/10.1002/jgrb.50247

Kim, Y.S., D.C.P. Peacock, and D.J. Sanderson. 2004. Fault damage zones. *Journal of Structural Geology* 26, no. 3: 503–517. https://doi.org/10.1016/j.jsg.2003.08.002

Knott, S.D., A. Beach, P.J. Brockbank, J. Lawson Brown, J.E. McCallum, and A.I. Welbon. 1996. Spatial and mechanical controls on normal fault populations. *Journal of Structural Geology* 18, no. 2–3: 359–372. https://doi.org/10.1016/S0191-8141(96)80056-3

Manning, C.E., and S.E. Ingebritsen. 1999. Permeability of the continental crust: Implications of geothermal data and metamorphic systems. *Reviews of Geophysics* 37, no. 1: 127–150.

Mazurek, M. 1998. Geology of the Crystalline Basement of Northern Switzerland and Derivation of Geological Input Data for Safety Assessment Models.

Nicholson, C., and R. L. Wesson. 1990. *Earthquake Hazard Associated With Deep Well Injection – A Report to the U.S. Environmental Protection Agency*. U.S. Geological Survey Bulletin (Vol. 1951).

Ranjram, M., T. Gleeson, and E. Luijendijk. 2015. Is the permeability of crystalline rock in the shallow crust related to depth, lithology or tectonic setting? *Geofluids* 15, no. 1–2: 106–119. https://doi.org/10.1111/gfl.12098

Rinaldi, A.P., P. Jeanne, J. Rutqvist, F. Cappa, and Y. Guglielmi. 2014. Effects of fault-zone architecture on earthquake magnitude and gas leakage related to CO_2 injection in a multi-layered sedimentary system. *Greenhouse Gases: Science and Technology* 2, no. 6: 408–418. https://doi.org/10.1002/ghg

Rojstaczer, S.A., S.E. Ingebritsen, and D.O. Hayba. 2008. Permeability of continental crust influenced by internal and external forcing. *Geofluids* 8, no. 2: 128–139. https://doi.org/10.1111/j.1468-8123.2008.00211.x

Rutqvist, J., A.P. Rinaldi, F. Cappa, P. Jeanne, A. Mazzoldi, L. Urpi, Y. Guglielmi, and V. Vilarrasa. 2016. Fault activation and induced seismicity in geologic carbon storage - Lessons learned from recent modeling studies. *Journal of Rock Mechanics and Geotechnical Engineering* 8: 789–804. https://doi.org/10.1016/j.jrmge.2016.09.001

Sausse, J. 2002. Hydromechanical properties and alteration of natural fracture surfaces in the Soultz granite (Bas-Rhin, France). *Tectonophysics* 348, no. 1–3: 169–185. https://doi.org/10.1016/S0040-1951(01)00255-4

Sausse, J., and A. Genter. 2005. Types of permeable fractures in granite. *Geological Society, London, Special Publications* 240, no. 1: 1–14. https://doi.org/10.1144/gsl.sp.2005.240.01.01

Shapiro, S.A., E. Huenges, and G. Borm. 1997. Estimating the crust permeability from fluid-injection-induced seismic emission at the KTB site. *Geophysical Journal International* 131, no. 2: F15–F18. https://doi.org/10.1111/j.1365-246X.1997.tb01215.x

Stober, I., and K. Bucher. 2015. Hydraulic conductivity of fractured upper crust: Insights from hydraulic tests in boreholes and fluid-rock interaction in crystalline basement rocks. *Geofluids* 15, no. 1–2: 161–178. https://doi.org/10.1111/gfl.12104

Stober, I., and K. Bucher. 2006. Hydraulic properties of the crystalline basement. *Hydrogeology Journal* 15, no. 2: 213–224. https://doi.org/10.1007/s10040-006-0094-4

Theis, C.V. 1935. The relation between the lowering of the piezometric surface and the rate and duration of discharge of a well using ground water storage. *Eos, Transactions American Geophysical Union* 16, no. 2: 519–524.

Townend, J., and M.D. Zoback. 2000. How faulting keeps the crust strong. *Geology* 28, no. 5: 399–402.

Walsh, F.R., and M.D. Zoback. 2016. Probabilistic assessment of potential fault slip related to injection-induced earthquakes: Application to north-central Oklahoma, USA. *Geology* 44, no. 12: 1–4. https://doi.org/10.1130/G38275.1

Walsh, F.R., and M.D. Zoback. 2015. Oklahoma's recent earthquakes and saltwater disposal. *Science Advances* 1500195, no. June: 1–9. https://doi.org/10.1126/sciadv.1500195

Wibberley, C.A.J., and T. Shimamoto. 2002. Internal structure and permeability of major strike-slip fault zones: The median tectonic line in Mie prefecture, Southwest Japan. *Journal of Structural Geology* 25, no. 1: 59–78. https://doi.org/10.1016/S0191-8141(02)00014-7

Yeck, W.L., M. Weingarten, H.M. Benz, D.E. McNamara, E.A. Bergman, R.B. Herrmann, J.L. Rubinstein, and P.S. Earle. 2016. Far-field pressurization likely caused one of the largest injection induced earthquakes by reactivating a large pre-existing basement fault structure. *AGU Publications - Geophysical Research Letters* February: 198–207. https://doi.org/10.1002/2016GL070861

Zhang, Y., S.S. Edel, J. Pepin, M.A. Person, R. Broadhead, J.P. Ortiz, S.L. Bilek, P.S. Mozley, and J.P. Evans. 2016. Exploring the potential linkages between oil-field brine reinjection, crystalline basement permeability, and triggered seismicity for the Dagger Draw Oil field, southeastern New Mexico, USA, using hydrologic modeling. *Geofluids* 16, 1–17. https://doi.org/10.1111/gfl.12199

Zhang, Y., M.A. Person, J.A. Rupp, K.M. Ellett, M.A. Celia, C.W. Gable, B. Bowen, J.P. Evans, K. Bandilla, P.S. Mozley, T. Dewers, and T. Elliot. 2013. Hydrogeologic controls on induced seismicity in crystalline basement rocks due to fluid injection into basal reservoirs. *Groundwater* 51, no. 4: 525–538. https://doi.org/10.1111/gwat.1207